Fuel Cells

DOI: 10.1002/anie.201408210

# Rational Design of Lower-Temperature Solid Oxide Fuel Cell Cathodes via Nanotailoring of Co-Assembled Composite Structures**

*Kang Taek Lee, Ashley A. Lidie, Hee Sung Yoon, and Eric D. Wachsman**

***Abstract:*** *A novel in situ co-assembled nanocomposite LSM-$Bi_{1.6}Er_{0.4}O_3$ (ESB) (icn-LSMESB) was obtained by conjugated wet-chemical synthesis. It showed an enhancement of the cathode polarization at 600°C by >140 times relative to conventional LSM-$Y_{0.08}Zr_{0.84}O_{1.92}$ (YSZ) cathodes and exceptional solid oxide fuel cell (SOFC) performance of >2 $W cm^{-2}$ below 750°C. This demonstrates that this novel cost-effective and broadly applicable process provides new opportunities for performance enhancement of energy storage and conversion devices by nanotailoring of composite electrodes.*

Solid oxide fuel cells (SOFCs) have tremendous potential due to having the highest fuel to electricity conversion efficiency[1] as well as unique fuel flexibility,[2] allowing the use of various types of hydrocarbon fuels (including biomass) and hydrogen, and thus providing a critical energy solution.[3] Lowering the SOFC operating temperature below 800°C is critical to reduce the system costs and performance degradation rates, enhance the durability and thermal cycling as well as shorten the start-up time, resulting in new opportunities in personal power and transportation markets.[1]

Achieving high performance SOFCs at reduced temperature is impeded primarily by increased cathode polarization resistance due to the thermally activated nature of the oxygen reduction reaction (ORR).[4]

Recently cobaltite-based perovskite materials (e.g., $Ba_{1-x}Sr_xCo_{1-y}Fe_yO_3$ (BSCF))[5] have been highlighted due to their mixed ionic and electronic conducting (MIEC) character and oxygen reduction reaction (ORR) activity at reduced temperature.[5,6] However, their practical applications are limited by reactivity with the most widely used yttria-stabilized zirconia (YSZ) electrolytes[7] and questionable long-term stability due to $CO_2$ poisoning[8] and Sr segregation.[9]

[*] Prof. K. T. Lee, A. A. Lidie, Dr. H. S. Yoon, Prof. E. D. Wachsman
University of Maryland Energy Research Center (UMERC)
University of Maryland
College Park, Maryland, 20742 (USA)
E-mail: ewach@umd.edu
Prof. K. T. Lee
Department of Energy Systems Engineering
Daegu Gyeongbuk Institute of Science and Technology (DGIST)
50-1 Sang-Ri, Hyeongpung-Myeon, Dalseong-Gun, Daegu (Korea)

[**] We acknowledge the support of the University of Maryland Energy Research Center (UMERC), Redox Power Systems, and Maryland NanoCenter and its NispLab. The NispLab is supported in part by the NSF as a MRSEC Shared Experimental Facility. A. Lidie acknowledges support from the SMART Scholarship.

Supporting information for this article is available on the WWW under http://dx.doi.org/10.1002/anie.201408210.

In contrast, at reduced temperature (<800°C) conventional $La_{1-x}Sr_xMnO_3$ (LSM) demonstrates high stability during long-term operation and compatibility with most SOFC electrolytes including YSZ,[10] but has low electrocatalytic activity due to negligible oxygen ion conductivity. Recent oxygen in situ isotope exchange (IIE) studies of LSM show that there is no energy barrier for dissociative adsorption of oxygen on the surface, as evident by the apparent negative activation energy for oxygen exchange.[11]

Stabilized bismuth oxides in the fluorite structure have exceptionally high ionic conductivity and ORR rate. For example, the oxygen ion conductivity of 20 mol%-doped erbia-stabilized bismuth oxide (ESB) at 500°C (0.0268 $S cm^{-1}$) is 30 times greater than that of YSZ (0.0009 $S cm^{-1}$).[12] Moreover, bismuth oxides have a remarkably high oxygen surface exchange coefficient ($k_s$), which is much higher (by a factor of $10^3$ at 700°C) than that of YSZ[13] and even competitive with that of the highest performance cobaltite-based perovskite cathodes.[14]

Although the ORR involves multiple mechanistic steps from oxygen adsorption to incorporation into the electrolyte lattice at electrochemically active triple-phase boundaries (TPBs), it can be more simply described by two major rate-limiting steps as follows:[15]

$$\text{Step 1 : Dissociated adsorption : } O_2(g) + 2S \underset{k_{-1}}{\overset{k_1}{\leftrightarrow}} 2O_{ad}$$

$$\text{Step 2 : Oxygen incorporation : } O_{ads} + V_o \underset{k_{-2}}{\overset{k_2}{\leftrightarrow}} O_o + S$$

where $O_{ads}$ is a surface adsorbed oxygen, $O_o$ a lattice oxygen in the surface layer, $V_o$ a surface oxygen vacancy (empty), and $S$ a surface site. $k_1$, $k_{-1}$, $k_2$, and $k_{-2}$ are reaction-rate constants.

Thus, toward a rational design of SOFC cathodes we integrated the superior dissociative adsorption (step 1) property of LSM surfaces with the superior oxygen incorporation (step 2) of highly conductive stabilized bismuth oxides[16] by a co-assembled ESB-LSM nanocomposite particle, as illustrated in Figure 1a. Moreover, this well-tailored nanostructure results in highly extended electrochemically active TPBs in the 3D porous cathode bulk.

However, the development of dual-phase nanocomposite particles comprised of multicomponent ceramics, is extremely challenging due to their high surface area (thus, high surface energy), leading to micron-size agglomeration of each phase's particles in the initial stage of mixing combined with intercomponent reaction during sintering at high temperature.

Therefore, we developed an in situ co-assembly process for the nanocomposite $La_{0.8}Sr_{0.2}MnO_3$ (LSM)-$Bi_{1.6}Er_{0.4}O_3$

  

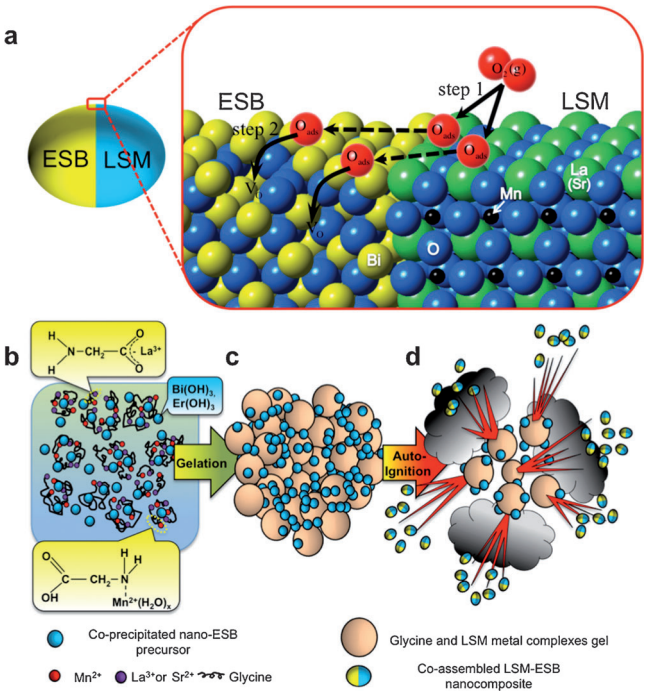


***Figure 1.*** a) Proposed rational design of a SOFC cathode nanocomposite particle consisting of a half ESB phase and a half LSM phase (left) and illustration of the two-step ORR mechanism with superior oxygen dissociative adsorption on LSM surface and fast oxygen incorporation into ESB phase (right). Color code: red, O ions from air; blue, lattice O ions; yellow, Bi ions; black, Mn ions; green, La (or Sr) ions. The dotted arrows indicate oxygen ion diffusion on the nanoparticle surface. Conceptual diagram of the novel in situ co-assembled nanocomposite process: b) molecular level mixing of the coprecipitated ESB precursors consisting of $Bi(OH)_3$ and $Er(OH)_3$ with glycine and LSM–metal complexes; c) water drying and gelation; d) auto-ignition by glycine–nitrate combustion.

(ESB) through uniquely conjugated reverse-strike coprecipitation and glycine-nitrate combustion (GNC) at extremely low temperature ($<300\,°C$).

A conceptual process diagram is shown in Figure 1 b–d and a more in-depth experimental description is discussed in the method section and Figure S1. To preclude intercomponent reactions between LSM and ESB (e.g., $Sr^{3+}$ and $Bi^{3+}$) during the synthesis process, "flower-like" high surface area nanoESB precursor precipitates (Figure S2) of $Bi(OH)_3$ and $Er(OH)_3$ confining $Bi^{3+}$ and $Er^{3+}$ were preformed by a reverse-strike coprecipitation. To synthesize the nanoLSM phase, metal nitrates of La, Sr, and Mn were dissolved with amino acid and glycine in an aqueous solution. Due to its zwitterionic nature, glycine acts as the chelating agent with two different functional end groups: carboxylic acid and amine, which capture the metal ions to form glycine–metal complexes[17] (insets in Figure 1 b). The ESB precursors are added to the above solution and, due to the nature of the aqueous solution, the glycine–LSM cation complexes act as spacers between high surface ESB precursor particles, resulting in a molecular level mixture of the two groups of metal ions as shown schematically in Figure 1 b. As the water evaporates, the glycine–metal cation complexes experience gelation, and the structure becomes ESB precursor particles embedded in a glycine–LSM metal complex gel (Figure 1 c). Upon heating to ca. 300 °C, this gel structure auto-ignites through the GNC mechanism in less than 3 s with high exothermicity, producing in situ co-assembled nanocomposites of LSM–ESB (referred to as icn-LSMESB) as shown in Figure 1 d.

X-ray diffraction (XRD) analysis (upper spectrum in Figure 2 a) reveals that the as-synthesized powders are fully crystallized for both LSM and ESB phases with minor peaks of unreacted $Bi(OH)_3$. Moreover, there is no evidence for any interreaction between the two phases, indicating successful in situ crystallization of selective components for dual-phase formation.

On the basis of the propellant chemistry[18] the stoichiometric redox reaction between the oxidizer (LSM metal nitrates) and fuel (glycine), which is responsible for the crystallization of LSM, was calculated (see the Supporting Information, SI). We started the process with a G/N ratio of 0.54, which is close to the stoichiometric ratio (0.56). In situ crystallization of the ESB phase is attributed to the short-range atomic movement within ESB precursors through fast calcination ($<3$ s) due to the adiabatic flame heat from the GNC reaction, which effectively prevents any interreaction with the LSM components. We further annealed the as-synthesized LSM–ESB up to 800 °C to simulate actual SOFC operating conditions ($\leq 750\,°C$) and confirmed the compatibility and stability of both phases (middle spectrum in Figure 2 a), demonstrating the suitability for SOFC applications. However, without glycine the auto-ignition did not occur and we observed secondary phase formation between $Bi^{3+}$ and $Sr^{2+}$ ($SrBi_4O_7$) as shown in the lower spectrum in Figure 2 a, indicating that the auto-ignition step plays a critical role for in situ crystallization of multicomponent, dual-phase composites.

Figure 2 b shows the XRD patterns of LSM–ESB samples with different G/N ratios after annealing at 800 °C. The results indicate that a G/N ratio of $\geq 0.54$ produces enough thermal energy both to oxidize LSM nitrates and to crystallize ESB precursors. Based on the redox reactions with various G/N ratios, the effect of the glycine amount (i.e., G/N ratio) was estimated from the enthalpy of combustion and the corresponding adiabatic flame temperature and the results are plotted in Figure 2 c (see SI and Table S2).

It is noted that the actual flame temperature values are expected to be somewhat lower than the calculated ones due to radiative heat losses and incomplete redox reactions. Nevertheless, actual experimental combustion photos of the highest flame for each G/N ratio (insets of Figure 2 c) visually confirm how the glycine amount impacts the adiabatic flame temperature. Moreover, this result is in good agreement with the recently reported minimum calcination temperatures of nanoESB obtained by co-precipitation ($\approx 500\,°C$).[16] The crystallite size (L) of the ESB phases with various G/N ratios was estimated (Figure 2 c) from the highest intensity (111) peaks from XRD patterns in Figure 2 b by the Scherrer equation,[19] clearly indicating a strong dependence of the ESB crystallite size on the G/N ratio. Thus, the above results demonstrate that the glycine–metal complexes act as "nano-furnaces" for the in situ calcination of ESB and the final

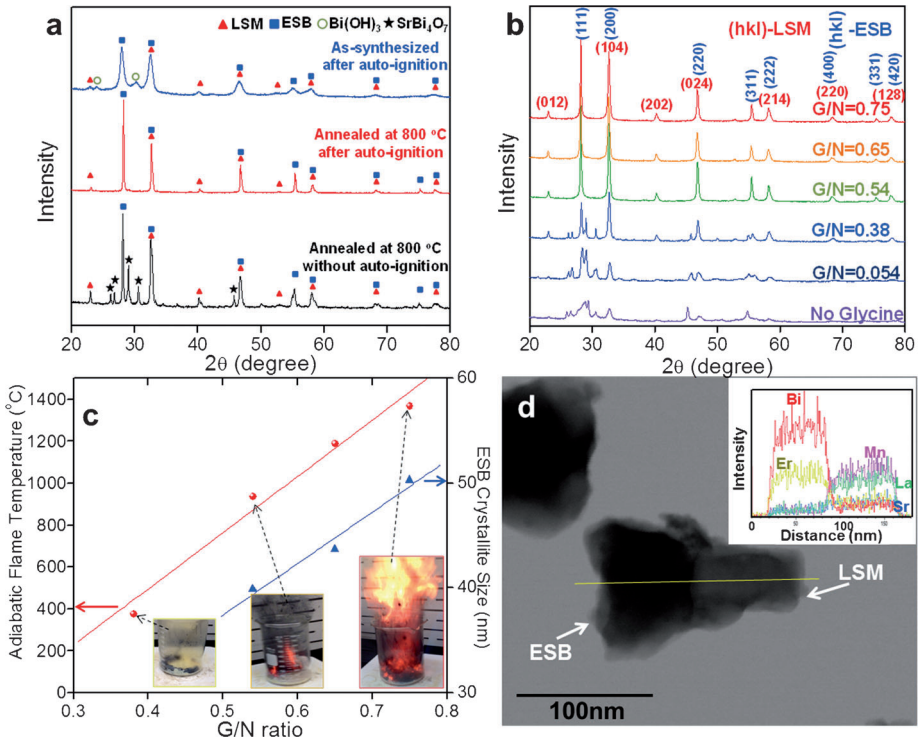


***Figure 2.*** a) X-ray diffractograms of as-synthesized (upper), annealed at 800 °C with auto-ignition (middle), and annealed at 800 °C without auto-ignition (lower) of icn-LSMESB powders. b) X-ray diffractograms of icn-LSMESB powders with various G/N ratios after annealing at 800 °C with auto-ignition. c) Adiabatic flame temperature (left *Y*-axis) and ESB crystallite size (right *Y*-axis) as a function of G/N ratio. Insets are still frames of highest fire flame during the process. d) TEM micrograph of icn-LSMESB particles with a G/N ratio of 0.54 after annealing at 800 °C. Inset is EDX line scan spectra along the yellow line in the TEM image.

product size is precisely controlled by the fuel (glycine) amount.

Figure 2d shows the representative structure of nanocomposite LSM–ESB particles synthesized with a G/N ratio = 0.54 obtained using transmission electron microscopy (TEM), which are very similar to the schematic diagram of the proposed co-assembled nanoparticle in Figure 1a. It is impressive that even after heat treatment at 800 °C, a nanoscale primary particle size was maintained at ca. 150 nm. We attribute this to the associated gas evolution during the GNC reaction (e.g., 26.3 mol of gas per 1 mol of LSM formation, Table S2) at the initial stage and prevention of grain growth by the dual-phase nature during the later annealing step. Moreover, we observed that these particles were dual-phase LSM and ESB nanoparticles without intermixing. Energy dispersive X-ray (EDX) line-scan analysis in scanning TEM (STEM) mode (upper inset in Figure 2d) clearly shows that the ESB and LSM are seamlessly co-assembled without any interaction. The particle size of the co-assembled ESB phase estimated from the TEM observation was ca. 70 nm, which is comparable to the value of ESB crystallite size (ca. 44 nm) from the XRD result in Figure 2c. Although the in-depth co-assembly mechanism is not yet conclusive, we believe that self-assembling between adjacent LSM and ESB particles involves an excess exothermic energy from the adiabatic flame temperature just after crystallization of each phase in the initial GNC step.

The polarization resistance of the icn-LSMESB cathode at reduced temperature was evaluated with icn-LSMESB | ESB | icn-LSMESB symmetric cells by electrochemical impedance spectroscopy (EIS). Figure 3a shows the Nyquist plots of the cells with the icn-LSMESB cathodes with the optimum G/N ratio of 0.54 (Figure S3) and 37 vol% LSM content (Figure S4) from 500 to 677 °C. For direct comparison, all impedance spectra were ohmic-resistance-subtracted.

The corresponding cathode area specific resistance (ASR) of icn-LSMESB was extremely low (e.g., 0.078 $\Omega\,cm^2$ at 600 °C), drastically reducing ASR by more than 140 times compared to conventional LSM–YSZ cathodes (e.g., 11.37 $\Omega\,cm^2$ at 600 °C;[20] (Figure 3b) and the lowest ASR reported to date for any LSM-based cathode with any microstructure (Figure S5). Moreover, the performance of icn-LSMESB is superior to that of many cobaltite-based high performance cathodes (e.g., 0.078 $\Omega\,cm^2$ for icn-LSMESB versus 0.27 $\Omega\,cm^2$ for $La_{1-x}Sr_xCo_{1-y}Fe_yO_3$–$Sm_{1-x}Sr_xCoO_3$ (LSCF–SSC) at 600 °C[6c]) and essentially identical to the state-of-the-art benchmark cathode, BSCF[5] (Figure 3b).

This result clearly demonstrates that our rational cathode design, based on co-assembled nanostructures of locally confined desired surface properties, dramatically enhances the ORR rate not only due to greatly extended electrochemically active TPB sites of a highly percolated dual-phase nanonetwork, but also due to the synergy between enhanced dissociative adsorption of oxygen by isolated LSM surface integrated with fast oxygen incorporation kinetics into ESB lattice as shown conceptually in Figure 1a.

Figure 3c shows the current–voltage (*I–V*) characterization of the icn-LSMESB cathode on a full-structured SOFC from 550 to 750 °C, yielding exceptionally high performance in peak power density at reduced temperature (2.0 $W\,cm^{-2}$ at 750 °C and 1.8 $W\,cm^{-2}$ at 700 °C) compared to the recently reported YSZ-based SOFC performance (e.g., $<1\,W\,cm^{-2}$ at 700 °C)[23] with similar electrolyte and anode architectures. Further reduction of the SOFC operation temperature with even higher output power density is achievable if the icn-LSMESB is combined with other advanced SOFC components (e.g., highly conductive, functionally graded ceria/bismuth oxide bilayered electrolytes,[1] ultrathin (>100 nm) YSZ electrolytes obtained by chemical solution deposition,[24] or bimodally integrated anode functional layers[25]).

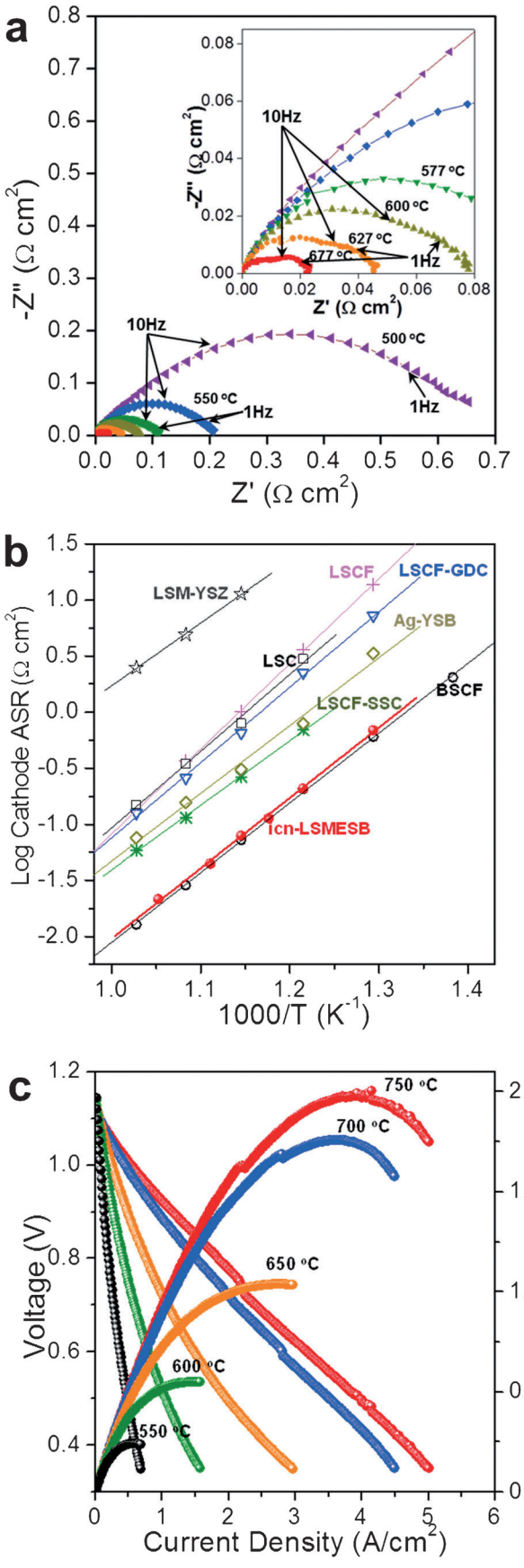


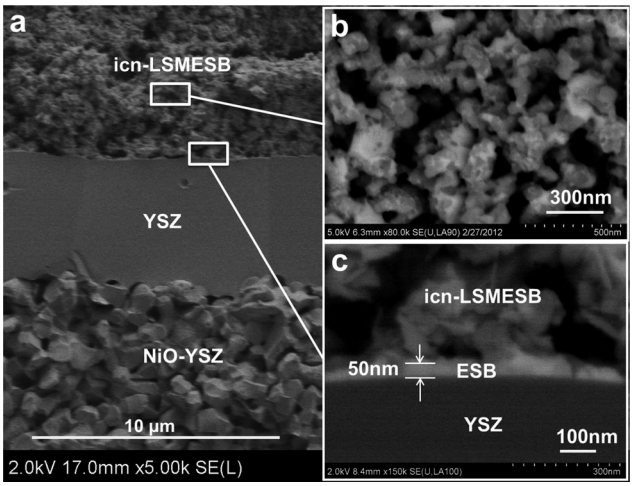


***Figure 4.*** SEM images of a) icn-LSMESB-(cathode) | YSZ(electrolyte) | NiO-YSZ(anode) structures, and magnified images of b) icn-LSMESB cathode and c) cathode/electrolyte interface.

Figure 4 shows scanning electron microscopy (SEM) micrographs of the SOFC with Ni–YSZ | YSZ | icn-LSMESB multilayers after *I–V* testing. There was no detectable reactivity or interfacial diffusion between icn-LSMESB and YSZ based on XRD (Figure S6) and EDX mapping (Figure S7). As shown in Figure 4a, all layers are well-established with a dense YSZ electrolyte (ca. 7 μm) responsible for the high open-circuit voltage (OCV; Figure 3c). However, the exceptionally high power densities should be attributed primarily to the co-assembled nanostructural features of the ca. 30 μm thick icn-LSMESB cathode. Magnified SEM morphology of the icn-LSMESB in backscattered mode (Figure 4b) shows that both LSM and ESB phases are homogeneously intermixed with high 3D connectivity of each phase and the average particle size is less than ca. 200 nm, similar to the primary particle size (ca. 150 nm) shown in Figure 2d, indicating that the co-assembled dual-phase composite structure effectively prevents grain growth of the other phase during sintering. This observed nanostructure of the icn-LSMESB justifies the extremely low ASRs (Figure 3b) and the ORR enhancement mechanism, as explained above, as well as the resulting high power density of the SOFC (Figure 3c).

Moreover, we observed another striking feature of the icn-LSMESB cathode on the YSZ electrolyte: the self-assembly of a continuous nanoscale ESB layer (ca. 50 nm)

***Figure 3.*** a) Nyquist plots of an icn-LSMESB | ESB | icn-LSMESB symmetric cell at the temperature range from 500 to 677 °C. b) Arrhenius plots of conductivity of icn-LSMESB compared with the conventional $La_{0.8}Sr_{0.2}MnO_3$ (LSM)–YSZ cathodes[20] and the state-of-the-art high performance cathodes including $La_{0.6}Sr_{0.4}Co_{0.5}Fe_{0.5}O_{3-\delta}$ (LSCF),[6a] $La_{0.58}Sr_{0.40}CoO_{3-\delta}$ (LSC),[21] $La_{0.6}Sr_{0.4}Co_{0.5}Fe_{0.5}O_{3-\delta}$–$Gd_{0.2}Ce_{0.8}O_{3-\delta}$ (LSCF–GDC),[6b] Ag–$Y_{0.25}Bi_{0.75}O_{1.5}$ (Ag–YSB),[22] $La_{0.6}Sr_{0.4}Co_{0.5}Fe_{0.5}O_{3-\delta}$–$Sm_{0.5}Sr_{0.5}CoO_{3-\delta}$ (LSCF–SSC),[6c] and $Ba_{0.5}Sr_{0.5}Co_{0.8}Fe_{0.2}O_{3-\delta}$ (BSCF)[5] at reduced temperature. c) Current–voltage (*I–V*) characterization of the SOFC with icn-LSMESB(cathode) | YSZ(electrolyte) | NiO-YSZ(anode) structure at the temperature range from 550 to 750 °C.

at the cathode/electrolyte interface (Figure 4c and Figure S7). The formation of the extremely thin ESB layer can be explained by the high wettability and greater mobility by surface and lattice diffusion due to the lower melting temperature of bismuth oxide (ca. 827 °C) as compared to the melting temperature of LSM and YSZ (> 2000 °C). We believe this self-assembled nanoESB layer acts as an ESB/YSZ bilayered electrolyte, significantly improving the SOFC performance due to enhanced oxygen incorporation at the icn-LSMESB/ESB interface as recently demonstrated.[19]

In summary, in order to achieve a rationally designed LT-SOFC cathode based on desired ORR material properties, we developed a novel in situ co-assembly of multicomponent, dual-phase nanocomposites by uniquely conjugated wet chemical processes. Through nanoengineering, the desired surface properties of both phases were successfully isolated in the nanoregime (< 80 nm), resulting in outstanding SOFC cathode performance at lower temperatures. Thus, we believe this intelligent nanoarchitecture is promising for electrochemical performance enhancement of composite electrodes with broad applications in energy storage and conversion devices.

Received: August 13, 2014
Published online: October 6, 2014

**Keywords:** co-assembly · electrocatalysts · nanocomposites · oxygen reduction reaction · solid oxide fuel cells

[1] E. D. Wachsman, K. T. Lee, *Science* **2011**, *334*, 935 – 939.
[2] a) E. P. Murray, T. Tsai, S. A. Barnett, *Nature* **1999**, *400*, 649 – 651; b) K. T. Lee, C. M. Gore, E. D. Wachsman, *J. Mater. Chem.* **2012**, *22*, 22405 – 22408; c) S. D. Park, J. M. Vohs, R. J. Gorte, *Nature* **2000**, *404*, 265 – 267; d) Y. H. Huang, R. I. Dass, Z. L. Xing, J. B. Goodenough, *Science* **2006**, *312*, 254 – 257; e) L. Yang, S. Z. Wang, K. Blinn, M. F. Liu, Z. Liu, Z. Cheng, M. L. Liu, *Science* **2009**, *326*, 126 – 129.
[3] E. D. Wachsman, C. A. Marlowe, K. T. Lee, *Energy Environ. Sci.* **2012**, *5*, 5498 – 5509.
[4] S. B. Adler, *Chem. Rev.* **2004**, *104*, 4791 – 4843.
[5] Z. P. Shao, S. M. Haile, *Nature* **2004**, *431*, 170 – 173.
[6] a) F. Deganello, V. Esposito, M. Miyayama, E. Traversa, *J. Electrochem. Soc.* **2007**, *154*, A89 – A96; b) E. Perry Murray, M. J. Sever, S. A. Barnett, *Solid State Ionics* **2002**, *148*, 27 – 34; c) X. Y. Lou, S. Z. Wang, Z. Liu, L. Yang, M. L. Liu, *Solid State Ionics* **2009**, *180*, 1285 – 1289; d) W. Zhou, Z. Shao, R. Ran, R. Cai, *Electrochem. Commun.* **2008**, *10*, 1647 – 1651.
[7] a) A. Petric, P. Huang, F. Tietz, *Solid State Ionics* **2000**, *135*, 719 – 725; b) A. Mai, M. Becker, W. Assenmacher, F. Tietz, D. Hathiramani, E. Ivers-Tiffee, D. Stover, W. Mader, *Solid State Ionics* **2006**, *177*, 1965 – 1968.
[8] E. Bucher, A. Egger, G. B. Caraman, W. Sitte, *J. Electrochem. Soc.* **2008**, *155*, B1218 – B1224.
[9] D. Oh, D. Gostovic, E. D. Wachsman, *J. Mater. Res.* **2012**, *27*, 1992 – 1999.
[10] a) E. P. Murray, T. Tsai, S. A. Barnett, *Solid State Ionics* **1998**, *110*, 235 – 243; b) S. P. Yoon, J. Han, S. W. Nam, T. H. Lim, I. H. Oh, S. A. Hong, Y. S. Yoo, H. C. Lim, *J. Power Sources* **2002**, *106*, 160 – 166.
[11] a) E. N. Armstrong, K. L. Duncan, E. D. Wachsman, *Phys. Chem. Chem. Phys.* **2013**, *15*, 2298 – 2308; b) E. N. Armstrong, K. L. Duncan, D. J. Oh, J. F. Weaver, E. D. Wachsman, *J. Electrochem. Soc.* **2011**, *158*, B492 – B499.
[12] a) D. W. Jung, K. L. Duncan, E. D. Wachsman, *Acta Mater.* **2010**, *58*, 355 – 363; b) K. T. Lee, H. S. Yoon, E. D. Wachsman, *J. Mater. Res.* **2012**, *27*, 2063 – 2078.
[13] B. C. H. Steele, J. A. Kilner, P. F. Dennis, A. E. McHale, M. Vanhemert, A. J. Burggraaf, *Solid State Ionics* **1986**, *18 – 9*, 1038 – 1044.
[14] R. D. Bayliss, S. N. Cook, S. Kotsantonis, R. J. Chater, J. A. Kilner, *Adv. Energy Mater.* **2014**, *4*, 1301575.
[15] a) C. C. Kan, H. H. Kan, F. M. Van Assche, E. N. Armstrong, E. D. Wachsman, *J. Electrochem. Soc.* **2008**, *155*, B985 – B993; b) C. C. Kan, E. D. Wachsman, *J. Electrochem. Soc.* **2009**, *156*, B695 – B702; c) C. C. Kan, E. D. Wachsman, *Solid State Ionics* **2010**, *181*, 338 – 347.
[16] K. T. Lee, A. A. Lidie, S. Y. Jeon, G. T. Hitz, S. J. Song, E. D. Wachsman, *J. Mater. Chem. A* **2013**, *1*, 6199 – 6207.
[17] L. A. Chick, L. R. Pederson, G. D. Maupin, J. L. Bates, L. E. Thomas, G. J. Exarhos, *Mater. Lett.* **1990**, *10*, 6 – 12.
[18] S. R. Jain, K. C. Adiga, V. R. P. Verneker, *Combust. Flame* **1981**, *40*, 71 – 79.
[19] K. T. Lee, D. W. Jung, H. S. Yoon, A. A. Lidie, M. A. Camaratta, E. D. Wachsman, *J. Power Sources* **2012**, *220*, 324 – 330.
[20] E. Perry Murray, S. A. Barnett, *Solid State Ionics* **2001**, *143*, 265 – 273.
[21] F. Han, R. Muecke, T. Van Gestel, A. Leonide, N. H. Menzler, H. P. Buchkremer, D. Stover, *J. Power Sources* **2012**, *218*, 157 – 162.
[22] C. R. Xia, Y. Zhang, M. L. Liu, *Appl. Phys. Lett.* **2003**, *82*, 901 – 903.
[23] D. Yoon, J.-J. Lee, H.-G. Park, S.-H. Hyun, *J. Electrochem. Soc.* **2010**, *157*, B455 – B462.
[24] E.-O. Oh, C.-M. Whang, Y.-R. Lee, S.-Y. Park, D. H. Prasad, K. J. Yoon, J.-W. Son, J.-H. Lee, H.-W. Lee, *Adv. Mater.* **2012**, *24*, 3373 – 3377.
[25] K. T. Lee, H. S. Yoon, J. S. Ahn, E. D. Wachsman, *J. Mater. Chem.* **2012**, *22*, 17113 – 17120.

  